



HAL
open science

Automatic two-plane balancing for rigid rotors

D.J. Rodrigues, A.R. Champneys, M.I. Friswell, R.E. Wilson

► **To cite this version:**

D.J. Rodrigues, A.R. Champneys, M.I. Friswell, R.E. Wilson. Automatic two-plane balancing for rigid rotors. *International Journal of Non-Linear Mechanics*, 2008, 43 (6), pp.527. 10.1016/j.ijnonlinmec.2008.01.002 . hal-00501776

HAL Id: hal-00501776

<https://hal.science/hal-00501776>

Submitted on 12 Jul 2010

HAL is a multi-disciplinary open access archive for the deposit and dissemination of scientific research documents, whether they are published or not. The documents may come from teaching and research institutions in France or abroad, or from public or private research centers.

L'archive ouverte pluridisciplinaire **HAL**, est destinée au dépôt et à la diffusion de documents scientifiques de niveau recherche, publiés ou non, émanant des établissements d'enseignement et de recherche français ou étrangers, des laboratoires publics ou privés.

Author's Accepted Manuscript

Automatic two-plane balancing for rigid rotors

D.J. Rodrigues, A.R. Champneys, M.I. Friswell,
R.E. Wilson

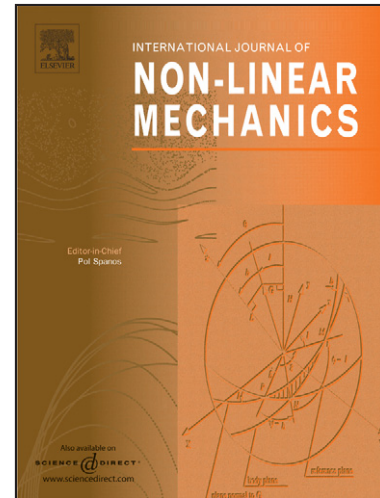
PII: S0020-7462(08)00015-2
DOI: doi:10.1016/j.ijnonlinmec.2008.01.002
Reference: NLM 1441

To appear in: *International Journal of Non-Linear Mechanics*

Received date: 25 May 2007
Revised date: 25 November 2007
Accepted date: 4 January 2008

Cite this article as: D.J. Rodrigues, A.R. Champneys, M.I. Friswell and R.E. Wilson, Automatic two-plane balancing for rigid rotors, *International Journal of Non-Linear Mechanics* (2008), doi:10.1016/j.ijnonlinmec.2008.01.002

This is a PDF file of an unedited manuscript that has been accepted for publication. As a service to our customers we are providing this early version of the manuscript. The manuscript will undergo copyediting, typesetting, and review of the resulting galley proof before it is published in its final citable form. Please note that during the production process errors may be discovered which could affect the content, and all legal disclaimers that apply to the journal pertain.



www.elsevier.com/locate/nlm

Automatic Two-Plane Balancing for Rigid Rotors

D.J. Rodrigues^{a,*}, A.R. Champneys^a, M.I. Friswell^b and R.E. Wilson^a

^a*Department of Engineering Mathematics, ^bDepartment of Aerospace Engineering,
University of Bristol, Bristol, BS8 1TR, UK*

Abstract

We present an analysis of a two-plane automatic balancing device for rigid rotors. Ball bearings, which are free to travel around a race, are used to eliminate imbalance due to shaft eccentricity or misalignment. The rotating frame is used to derive autonomous equations of motion and the symmetry breaking bifurcations of this system are investigated. Stability diagrams in various parameter planes show the coexistence of a stable balanced state with other less desirable dynamics.

1 Introduction

The primary cause of vibration in rotating machinery is mass imbalance, which occurs when the principal axis of the moment of inertia is not coincident with the axis of rotation. In the case of a rigid rotor the usual balancing procedure involves adding or subtracting correction masses in two distinct planes so that the principal axis is re-centred and realigned. However, effects such as thermal deformation and material erosion can cause the rotor's mass distribution to change, and in such circumstances the balancing procedure may have to be repeated. This limitation motivates the study of self-compensating balancing devices, in which masses redistribute themselves so as to eliminate any imbalance.

One such device is the automatic ball balancer (ABB), which consists of a series of balls that are free to travel around a race which is filled with a viscous fluid. The first study of an ABB was carried out by Thearle in 1932 [1], and the existence of a stable steady state at rotation speeds above the first critical frequency was demonstrated. More recently, the equations of motion for a planar Jeffcott rotor with an ABB have been derived using Lagrange's method [2, 3, 4]. In particular Green et al. [4] use rotating coordinates to obtain an autonomous system of governing equations. The stability boundaries for the fully nonlinear system are then computed using numerical continuation techniques.

In 1977, Hedaya and Sharp [5] extended the autobalancing concept by proposing a two-plane device that would be able to compensate for both shaft eccentricity and shaft misalignment, see Fig. 1. However, the ABB models which are based on a Jeffcott rotor are unable to explain phenomena that are related to shaft misalignment as they do not include any tilting motions. These out-of-plane motions are considered in the studies of Chung and Jang [6], Chao et al. [7] and Sperling et al. [8], but only linear stability analyses are provided. Here we extend the planar analysis of [4] so that we may model the tilting motion of the ABB and analyse the two-plane automatic balancer for rigid rotors.

The rest of this paper is organised as follows. In section 2 we use rotating coordinates to derive autonomous equations of motion for the ABB. The steady states of the system are considered in section 3, and we focus on using numerical bifurcation theory to investigate the effect that the physical parameters have on the stability of the balanced state. In section 4 we supplement the findings of the bifurcation analysis by providing numerical simulations of the dynamics, and investigating the effect of the initial conditions. Finally, in section 5 we draw conclusions and discuss possible directions for future work.

*Corresponding author. E-mail: david.rodrigues@bristol.ac.uk

2 Derivation of the Equations of Motion

In this section, we derive an autonomous system of governing equations for the automatic balancer by describing the position of the rotor centre with respect to rotating coordinates and applying Lagrange's method [3, 4, 6]. For a background to the rotordynamics theory see for example [9].

2.1 Mechanical Setup

The mechanical device that we wish to model is illustrated in Fig. 1, and is based on a rigid rotor which has been fitted with a two-plane automatic balancer [5, 8]. The rotor has mass M , moment of inertia tensor J , and is mounted on two compliant linear bearings which are located at S_1 and S_2 . The automatic balancer consists of a pair of races that are set normal to the shaft in two separate planes. Each race contains two balancing balls of mass m , which move through a viscous fluid and are free to travel, at a fixed distance R from the shaft axis. The position of the i th ball is specified by the axial and angular displacements z_i and α_i , which are written with respect to the $C\xi\eta z$ rotor axes.

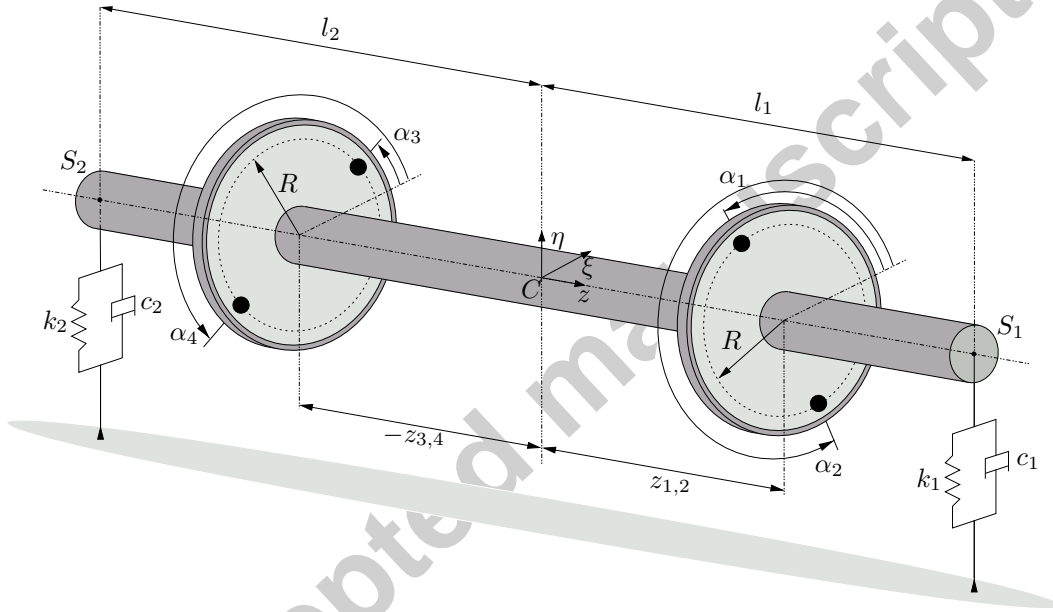


Fig. 1: Schematic diagram of a two-plane automatic balancer.

2.2 Co-ordinate frames

In order to describe the position and orientation of the rotor, it is helpful to consider the following frames of reference, as shown in Fig. 2. We begin with an inertial *space* frame $OXYZ$ with origin at O and Z -axis oriented along the undeflected bearing centreline. A rotation about the Z axis by the spin angle θ results in the *rotating* frame $OxyZ$. This transformation can be written as

$$\mathbf{x} = \mathbf{R}_1 \mathbf{X},$$

where \mathbf{x} and \mathbf{X} are the column vectors of coordinates in the rotating and inertial frames respectively, and

$$\mathbf{R}_1 = \begin{bmatrix} \cos \theta & \sin \theta & 0 \\ -\sin \theta & \cos \theta & 0 \\ 0 & 0 & 1 \end{bmatrix}.$$

The torsional behaviour of the rotor lies outside the scope of the present study, and so we shall only consider the special case of constant-speed operation, in which $\theta = \Omega t$.

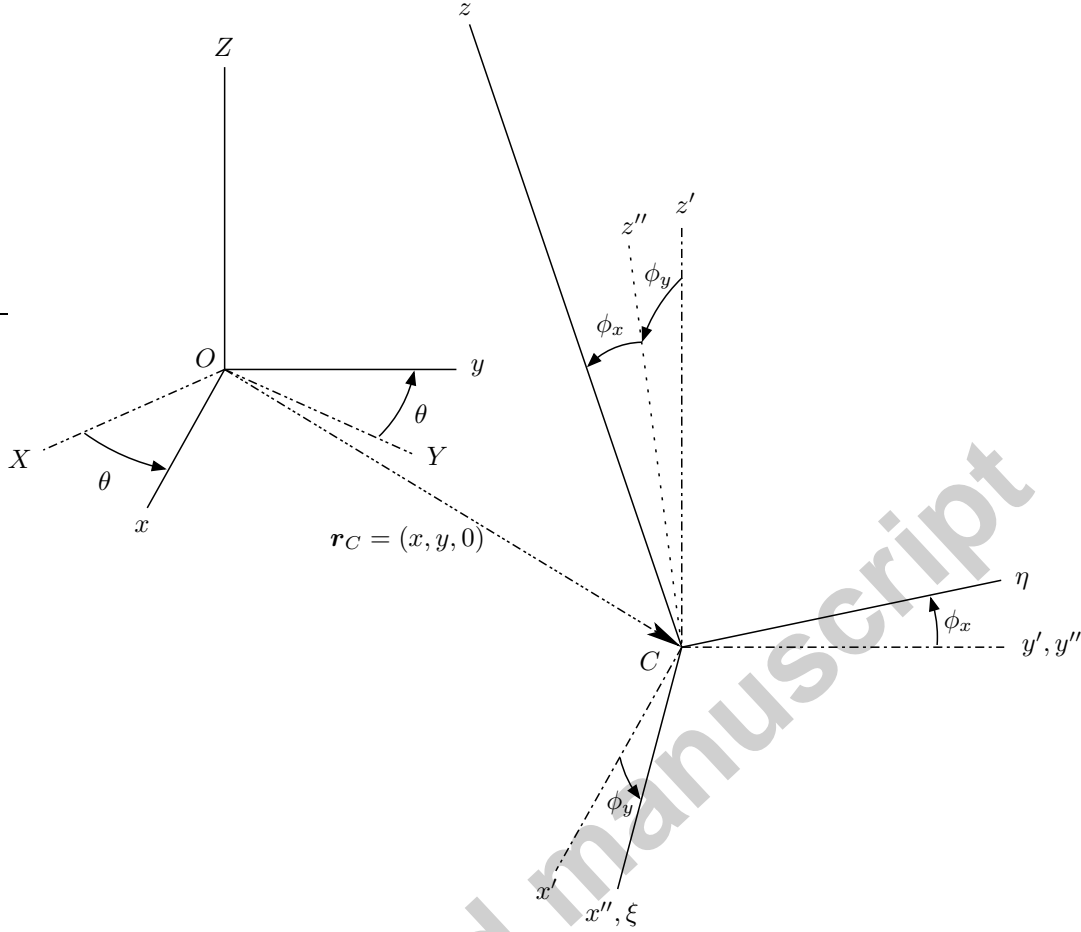


Fig. 2: Definition of the co-ordinate system.

The rotor's lateral motion can be described by introducing a frame $Cx'y'z'$ with origin at the geometric shaft centre C , and axes parallel to those of the rotating frame $OxyZ$. We neglect any motion in the axial direction, and so, the position vector of the geometric centre \mathbf{r}_C lies in the x - y plane. The rotor may also perform an out-of-plane tilting motion that can be described as follows: firstly we define an intermediate axes $Cx''y''z''$ related to $Cx'y'z'$ by a rotation of an angle ϕ_y about the y' axis, then we rotate $Cx''y''z''$ about x'' by an angle ϕ_x , which results in a *body* frame $C\xi\eta z$ that is fixed with respect to the rotor. These transformations can be combined to give

$$\boldsymbol{\xi} = \mathbf{R}_3 \mathbf{R}_2 \mathbf{x}', \quad (1)$$

where $\boldsymbol{\xi}$ and \mathbf{x}' are the co-ordinates in the body and primed axes respectively and

$$\mathbf{R}_2 = \begin{bmatrix} \cos \phi_y & 0 & -\sin \phi_y \\ 0 & 1 & 0 \\ \sin \phi_y & 0 & \cos \phi_y \end{bmatrix}, \quad \mathbf{R}_3 = \begin{bmatrix} 1 & 0 & 0 \\ 0 & \cos \phi_x & \sin \phi_x \\ 0 & -\sin \phi_x & \cos \phi_x \end{bmatrix}.$$

We are now able to transform between body coordinates and the space reference frame, however as shown in Fig. 3, small errors in the rotor's mass distribution will cause the body axes $C\xi\eta z$ to differ from the principal axes of the moment of inertia. The eccentricity ϵ , which gives rise to the static imbalance, is defined as the distance between the shaft centre C and the rotor's centre of mass G . Also the symmetry axis p_3 corresponding to the polar moment of inertia may be misaligned to the shaft axis by an angle χ , and this results in a couple imbalance. The symmetry of the rotor enables us to take the misalignment to be about the η axis without detracting from the generality of the model. The matrix expressing this

rotation is thus

$$\mathbf{R}_4 = \begin{bmatrix} \cos \chi & 0 & -\sin \chi \\ 0 & 1 & 0 \\ \sin \chi & 0 & \cos \chi \end{bmatrix},$$

and we also include the angle β , to denote the phase between the static and couple imbalances.

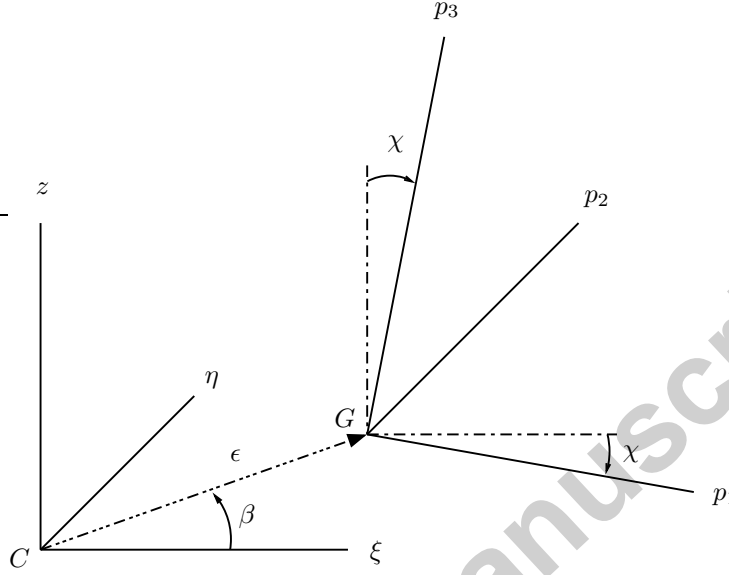


Fig. 3: Definition of the imbalance.

Before moving on to the derivation of the Lagrangian, it is worth noting that we have chosen the order of rotations so that the spin Ω is taken about the space Z axis as opposed to the body z axis. In the standard formulation for a linear four degree of freedom rotor, both approaches lead to equivalent equations of motion [9]. However, for our case where we must include the geometric nonlinearities due to the balancing balls, we find that autonomous equations can only be derived when Ω is taken about the space Z axis [10].

2.3 Lagrangian formulation

The nonlinear equations of motion for the system are derived from Lagrange's equations

$$\frac{d}{dt} \left(\frac{\partial T}{\partial \dot{q}_k} - \frac{\partial V}{\partial \dot{q}_k} \right) - \left(\frac{\partial T}{\partial q_k} - \frac{\partial V}{\partial q_k} \right) + \frac{\partial F}{\partial \dot{q}_k} = 0, \quad (2)$$

where T , and V , are the kinetic and potential energies respectively, F is Rayleigh's dissipation function and the q_k are the generalised co-ordinates. In our case the generalised coordinates are given by

$$\mathbf{q} = (x, y, \phi_x, \phi_y, \alpha_1, \alpha_2, \alpha_3, \alpha_4),$$

and so the motion is governed by a total of eight independent equations of motion. We proceed by deriving in turn the kinetic energy, the potential energy and Rayleigh's dissipation function.

2.3.1 Kinetic Energy

The kinetic energy of any rigid body can be decomposed as the sum of the translational energy of the centre of mass and the rotational energy of the body about its centre of mass. By treating the balls as points, the kinetic energy of the system can be written as

$$T = \frac{1}{2} M \dot{\mathbf{r}}_G^2 + \frac{1}{2} \boldsymbol{\Omega}^T \mathbf{J} \boldsymbol{\Omega} + \frac{1}{2} \sum_{i=1}^4 m \dot{\mathbf{r}}_{B_i}^2. \quad (3)$$

where $\dot{\mathbf{r}}_G$ and $\dot{\mathbf{r}}_{B_i}$ are the velocities of the rotor's centre of mass and the i th ball respectively, and $\boldsymbol{\Omega}$ is the angular velocity of the rotor. By using the inverse of the transformation defined in (1), we may write the position vector of the centre of mass, in the rotating frame as

$$\begin{aligned} \mathbf{r}_G &= \begin{bmatrix} x \\ y \\ 0 \end{bmatrix} + \mathbf{R}_2^T \mathbf{R}_3^T \begin{bmatrix} \epsilon \cos \beta \\ \epsilon \sin \beta \\ 0 \end{bmatrix}, \\ &= \begin{bmatrix} x + \epsilon (\cos \beta \cos \phi_y + \sin \beta \sin \phi_x \sin \phi_y) \\ y + \epsilon \sin \beta \cos \phi_x \\ \epsilon (-\cos \beta \sin \phi_y + \sin \beta \sin \phi_x \cos \phi_y) \end{bmatrix}. \end{aligned}$$

The rotating coordinates x and y have been chosen to describe the lateral motion because their use enables an autonomous formulation in which the spin angle Ωt does not explicitly enter into the governing equations.

The position vector of the i -th ball can be similarly given by

$$\begin{aligned} \mathbf{r}_{B_i} &= \begin{bmatrix} x \\ y \\ 0 \end{bmatrix} + \mathbf{R}_2^T \mathbf{R}_3^T \begin{bmatrix} R \cos \alpha_i \\ R \sin \alpha_i \\ z_i \end{bmatrix}, \\ &= \begin{bmatrix} x + R (\cos \phi_y \cos \alpha_i + \sin \phi_x \sin \phi_y \sin \alpha_i) + \cos \phi_x \sin \phi_y z_i \\ y + R \cos \phi_x \sin \alpha_i - \sin \phi_x z_i \\ R (-\sin \phi_y \cos \alpha_i + \sin \phi_x \cos \phi_y \sin \alpha_i) + \cos \phi_x \cos \phi_y z_i \end{bmatrix}. \end{aligned}$$

In contrast to the eccentricity ϵ , the race radius R cannot be assumed to be a small quantity. As a consequence, we must take extra care in terms relating to the ball positions when making any small angle assumptions on ϕ_x and ϕ_y . Thus, we prefer to compute the kinetic energy using the complete expressions for the displacements and make any approximations only after the equations of motion have been derived.

When calculating the translational kinetic energies, it is also necessary to express the velocities as they are seen by an observer in a space-fixed frame. Since we have written the position vectors with respect to rotating coordinates, we must use the following operator relation between derivatives to account for the change in frames

$$\left(\frac{d}{dt} \right)_s = \left(\frac{d}{dt} \right)_r + \boldsymbol{\Omega}_r \times \quad .$$

Here the subscripts s and r denote the time derivatives as seen by an observer in the space and rotating frames respectively, and $\boldsymbol{\Omega}_r = [0, 0, \Omega]^T$ is the angular velocity of the rotating frame with respect to an observer fixed in space. Hence, the velocity of the centre of mass in the space frame is given by

$$\begin{aligned} \dot{\mathbf{r}}_G &= \left(\frac{d\mathbf{r}_G}{dt} \right)_s = \left(\frac{d\mathbf{r}_G}{dt} \right)_r + \boldsymbol{\Omega}_r \times \mathbf{r}_G, \\ &= \begin{bmatrix} \dot{r}_{G,1} \\ \dot{r}_{G,2} \\ \dot{r}_{G,3} \end{bmatrix}, \end{aligned} \tag{4}$$

where

$$\begin{aligned} \dot{r}_{G,1} &= \dot{x} + \epsilon \left(-\cos \beta \sin \phi_y \dot{\phi}_y + \sin \beta \left(\cos \phi_x \dot{\phi}_x \sin \phi_y + \sin \phi_x \cos \phi_y \dot{\phi}_y \right) \right) - \Omega (y + \epsilon \sin \beta \cos \phi_x), \\ \dot{r}_{G,2} &= \dot{y} - \epsilon \sin \beta \sin \phi_x \dot{\phi}_x + \Omega (x + \epsilon (\cos \beta \cos \phi_y + \sin \beta \sin \phi_x \sin \phi_y)), \\ \dot{r}_{G,3} &= \epsilon \left(-\cos \beta \cos \phi_y \dot{\phi}_y + \sin \beta \left(\cos \phi_x \dot{\phi}_x \cos \phi_y - \sin \phi_x \sin \phi_y \dot{\phi}_y \right) \right). \end{aligned}$$

The velocities of the balls are computed in the same manner, so that

$$\dot{\mathbf{r}}_{B_i} = \begin{bmatrix} \dot{r}_{B_i,1} \\ \dot{r}_{B_i,2} \\ \dot{r}_{B_i,3} \end{bmatrix}, \tag{5}$$

with

$$\begin{aligned}
\dot{r}_{B_{i,1}} &= \dot{x} + R \left(-\sin \phi_y \dot{\phi}_y \cos \alpha_i - \cos \phi_y \sin \alpha_i \dot{\alpha}_i + \cos \phi_x \dot{\phi}_x \sin \phi_y \sin \alpha_i \right. \\
&\quad \left. + \sin \phi_x \cos \phi_y \dot{\phi}_y \sin \alpha_i + \sin \phi_x \sin \phi_y \cos \alpha_i \dot{\alpha}_i \right) + \left(-\sin \phi_x \dot{\phi}_x \sin \phi_y + \cos \phi_x \cos \phi_y \dot{\phi}_y \right) z_i \\
&\quad - \Omega (y + R \cos \phi_x \sin \alpha_i - \sin \phi_x z_i), \\
\dot{r}_{B_{i,2}} &= \dot{y} + R \left(-\sin \phi_x \dot{\phi}_x \sin \alpha_i + \cos \phi_x \cos \alpha_i \dot{\alpha}_i \right) - \cos \phi_x \dot{\phi}_x z_i \\
&\quad + \Omega (x + R (\cos \phi_y \cos \alpha_i + \sin \phi_x \sin \phi_y \sin \alpha_i) + \cos \phi_x \sin \phi_y z_i), \\
\dot{r}_{B_{i,3}} &= R \left(-\cos \phi_y \dot{\phi}_y \cos \alpha_i + \sin \phi_y \sin \alpha_i \dot{\alpha}_i + \cos \phi_x \dot{\phi}_x \cos \phi_y \sin \alpha_i - \sin \phi_x \sin \phi_y \dot{\phi}_y \sin \alpha_i \right. \\
&\quad \left. + \sin \phi_x \cos \phi_y \cos \alpha_i \dot{\alpha}_i \right) + \left(-\sin \phi_x \dot{\phi}_x \cos \phi_y - \cos \phi_x \sin \phi_y \dot{\phi}_y \right) z_i.
\end{aligned}$$

Next we turn to the expression for the rotational energy, which is most easily derived by using the principal axes $Gp_1p_2p_3$ of Fig. 3. It is in this frame that the inertia tensor \mathbf{J} , takes the diagonal form

$$\mathbf{J} = \begin{bmatrix} J_t & 0 & 0 \\ 0 & J_t & 0 \\ 0 & 0 & J_p \end{bmatrix},$$

in which J_t and J_p are the transverse and polar moments of inertia respectively. The angular velocity $\boldsymbol{\Omega}$ is composed from the following three angular velocity vectors: $\dot{\theta}$ directed along the Z-axis, $\dot{\phi}_y$ which is directed along the y' axis and $\dot{\phi}_x$ which lies along the x'' axis. The rotation matrices of Section 2.2 can now be used to transform these vectors so that they are written with respect to the principal axes, and taking the sum we obtain the angular velocity vector $\boldsymbol{\Omega}$ as

$$\begin{aligned}
\boldsymbol{\Omega} &= \mathbf{R}_4 \begin{bmatrix} \dot{\phi}_x \\ 0 \\ 0 \end{bmatrix} + \mathbf{R}_3 \begin{bmatrix} \dot{\phi}_y \\ 0 \\ 0 \end{bmatrix} + \mathbf{R}_3 \mathbf{R}_2 \mathbf{R}_1 \begin{bmatrix} 0 \\ 0 \\ \dot{\theta} \end{bmatrix}, \\
&= \begin{bmatrix} \cos \chi \left(\dot{\phi}_x - \dot{\theta} \sin \phi_y \right) - \sin \chi \left(-\dot{\phi}_y \sin \phi_x + \dot{\theta} \cos \phi_x \cos \phi_y \right) \\ \dot{\phi}_y \cos \phi_x + \dot{\theta} \sin \phi_x \cos \phi_y \\ \sin \chi \left(\dot{\phi}_x - \dot{\theta} \sin \phi_y \right) + \cos \chi \left(-\dot{\phi}_y \sin \phi_x + \dot{\theta} \cos \phi_x \cos \phi_y \right) \end{bmatrix}.
\end{aligned}$$

Hence the rotational energy can now be easily computed as

$$\begin{aligned}
\frac{1}{2} \boldsymbol{\Omega}^T \mathbf{J} \boldsymbol{\Omega} &= \frac{1}{2} J_t \left(\left(\cos \chi \left(\dot{\phi}_x - \Omega \sin \phi_y \right) - \sin \chi \left(-\dot{\phi}_y \sin \phi_x + \Omega \cos \phi_x \cos \phi_y \right) \right)^2 \right. \\
&\quad \left. + \left(\dot{\phi}_y \cos \phi_x + \Omega \sin \phi_x \cos \phi_y \right)^2 \right) \\
&\quad + \frac{1}{2} J_p \left(\sin \chi \left(\dot{\phi}_x - \Omega \sin \phi_y \right) + \cos \chi \left(-\dot{\phi}_y \sin \phi_x + \Omega \cos \phi_x \cos \phi_y \right) \right)^2.
\end{aligned} \tag{6}$$

Finally substituting the equations (4-6) into equation (3) completes the derivation of the kinetic energy for the system.

2.3.2 Potential Energy and Damping

The potential energy V , arises from the elastic deflection of the support bearings at S_1 and S_2 , as shown in Fig. 1. The coordinates of these supports are given in the rotor-fixed frame by $[0, 0, l_1]^T$ and $[0, 0, -l_2]^T$, and we assume that each bearing is linear and isotropic with stiffness k_1, k_2 and damping c_1, c_2 respectively. By transforming coordinates to the space frame, the deflection \mathbf{d}_{S_i} of each support may be written as

$$\begin{aligned} \mathbf{d}_{S_i} &= \mathbf{R}_1^T \begin{bmatrix} x \\ y \\ 0 \end{bmatrix} + \mathbf{R}_2^T \mathbf{R}_3^T \begin{bmatrix} 0 \\ 0 \\ \tilde{l}_i \end{bmatrix} - \begin{bmatrix} 0 \\ 0 \\ \tilde{l}_i \end{bmatrix}, \\ &= \begin{bmatrix} \cos \theta \left(x + \cos \phi_x \sin \phi_y \tilde{l}_i \right) - \sin \theta \left(y - \sin \phi_x \tilde{l}_i \right) \\ \sin \theta \left(x + \cos \phi_x \sin \phi_y \tilde{l}_i \right) + \cos \theta \left(y - \sin \phi_x \tilde{l}_i \right) \\ \cos \phi_x \cos \phi_y \tilde{l}_i - \tilde{l}_i \end{bmatrix}, \end{aligned}$$

where

$$\tilde{l}_1 = l_1 \quad \text{and} \quad \tilde{l}_2 = -l_2.$$

Hence the potential energy can be computed as

$$\begin{aligned} V &= \frac{1}{2} \sum_{i=1}^2 k_i \mathbf{d}_{S_i}^2, \\ &= \frac{1}{2} k_1 \left((x + \cos \phi_x \sin \phi_y l_1)^2 + (y - \sin \phi_x l_1)^2 + (\cos \phi_x \cos \phi_y l_1 - l_1)^2 \right) \\ &\quad + \frac{1}{2} k_2 \left((x - \cos \phi_x \sin \phi_y l_2)^2 + (y + \sin \phi_x l_2)^2 + (-\cos \phi_x \cos \phi_y l_2 + l_2)^2 \right). \end{aligned} \quad (7)$$

It is usual to assume that the vibrational coordinates (ϕ_x, ϕ_y) together with the imbalance errors ϵ and χ are small and $\mathcal{O}(\delta)$, with δ a small quantity. If we are to neglect terms of $\mathcal{O}(\delta^2)$ in the equations of motion, then all terms of order $\mathcal{O}(\delta^3)$ which enter into Lagrange's equation will not contribute to the system, and can be ignored. A routine calculation now gives the more familiar expression

$$V = \frac{1}{2} k_{11} (x^2 + y^2) + k_{12} (x\phi_y - y\phi_x) + \frac{1}{2} k_{22} (\phi_y^2 + \phi_x^2) + \mathcal{O}(\delta^3),$$

where

$$k_{11} = k_1 + k_2, \quad k_{12} = k_1 l_1 - k_2 l_2, \quad k_{22} = k_1 l_1^2 + k_2 l_2^2.$$

Next we turn to the dissipative effects, which arise from the damping at the supports, together with the viscous drag on the balls c_b , as they pass through the fluid in the race. These terms are most easily calculated through the use of Rayleigh's dissipation function

$$F = \frac{1}{2} \sum_{i=1}^2 c_i \dot{\mathbf{d}}_{S_i}^2 + \frac{1}{2} \sum_{i=1}^4 c_b \dot{\alpha}_i^2,$$

which after some manipulation we may write as

$$\begin{aligned} F &= \frac{1}{2} c_{11} \left((\dot{x} - \Omega y)^2 + (\dot{y} + \Omega x)^2 \right) \\ &\quad + c_{12} \left((\dot{x} - \Omega y) (\dot{\phi}_y + \Omega \phi_x) + (y + \Omega x) (-\dot{\phi}_x + \Omega \phi_y) \right) \\ &\quad + \frac{1}{2} c_{22} \left((\dot{\phi}_y + \Omega \phi_x)^2 + (-\dot{\phi}_x + \Omega \phi_y)^2 \right) + \frac{1}{2} \sum_{i=1}^4 c_b \dot{\alpha}_i^2 + \mathcal{O}(\delta^3), \end{aligned} \quad (8)$$

where

$$c_{11} = c_1 + c_2, \quad c_{12} = c_1 l_1 - c_2 l_2, \quad c_{22} = c_1 l_1^2 + c_2 l_2^2.$$

The fully geometric nonlinear equations of motion are generated by substituting (3), (7) and (8) into Lagrange's equations. Before displaying them here, we shall first continue with non-dimensionalisation.

2.3.3 Non-dimensionalisation and the Equations of Motion

We now consider the following dimensionless state variables

$$\bar{x} = \frac{x}{R}, \quad \bar{y} = \frac{y}{R}, \quad \bar{\phi}_x = \phi_x, \quad \bar{\phi}_y = \phi_y,$$

$$\bar{\alpha}_i = \alpha_i \quad \text{for } i = 1 \dots 4,$$

and the dimensionless time

$$\bar{t} = \Omega_1 t.$$

Here Ω_1 is the critical frequency associated with cylindrical whirl, and is given by, $\Omega_1 = \sqrt{k_{11}/M}$. Furthermore, we introduce the dimensionless parameters

$$\bar{\Omega} = \frac{\Omega}{\Omega_1}, \quad \bar{\epsilon} = \frac{\epsilon}{R}, \quad \bar{m} = \frac{m}{M}, \quad \bar{z} = \frac{z}{R},$$

$$\bar{J} = \frac{J}{MR^2}, \quad \bar{J}_p = \frac{J_p}{MR^2}, \quad \bar{\chi} = \chi, \quad \bar{c}_b = \frac{c_b}{m\Omega_1 R^2},$$

$$\bar{k}_{11} = \frac{k_{11}}{M\Omega_1^2} \equiv 1, \quad \bar{k}_{12} = \frac{k_{12}}{M\Omega_1^2 R}, \quad \bar{k}_{22} = \frac{k_{22}}{M\Omega_1^2 R^2},$$

$$\bar{c}_{11} = \frac{c_{11}}{M\Omega_1}, \quad \bar{c}_{12} = \frac{c_{12}}{M\Omega_1 R}, \quad \bar{c}_{22} = \frac{c_{22}}{M\Omega_1 R^2}.$$

The equations of motion with respect to these non-dimensional quantities are computed with the aid of the computer algebra system **Maple**, and are given as follows up to order $\mathcal{O}(\delta^2)$. The overbars have been omitted for clarity and we start with the equations for the rotor motion, which are

$$\begin{bmatrix} \mathbf{M} & \mathbf{0} \\ \mathbf{0} & \mathbf{M} \end{bmatrix} \ddot{\mathbf{x}} + \begin{bmatrix} \mathbf{C} & -\Omega(2\mathbf{M} - \mathbf{G}) \\ \Omega(2\mathbf{M} - \mathbf{G}) & \mathbf{C} \end{bmatrix} \dot{\mathbf{x}} + \begin{bmatrix} \mathbf{K} - \Omega^2(\mathbf{M} - \mathbf{G}) & -\Omega\mathbf{C} \\ \Omega\mathbf{C} & \mathbf{K} - \Omega^2(\mathbf{M} - \mathbf{G}) \end{bmatrix} \mathbf{x}$$

$$= \Omega^2 \begin{bmatrix} \epsilon \cos \beta \\ \chi(J_t - J_p) \\ \epsilon \sin \beta \\ 0 \end{bmatrix} + m \sum_{i=1}^4 \begin{bmatrix} (\Omega + \dot{\alpha}_i)^2 & 0 & \ddot{\alpha}_i & 0 \\ 0 & (\Omega + \dot{\alpha}_i)^2 & 0 & \ddot{\alpha}_i \\ -\ddot{\alpha}_i & 0 & (\Omega + \dot{\alpha}_i)^2 & 0 \\ 0 & -\ddot{\alpha}_i & 0 & (\Omega + \dot{\alpha}_i)^2 \end{bmatrix} \begin{bmatrix} \cos \alpha_i \\ z_i \cos \alpha_i \\ \sin \alpha_i \\ z_i \sin \alpha_i \end{bmatrix} + \begin{bmatrix} 0 \\ n_{\phi_y} \\ 0 \\ n_{-\phi_x} \end{bmatrix}. \quad (9)$$

where

$$\mathbf{M} = \begin{bmatrix} 1 + 4m & \sum_i m z_i \\ \sum_i m z_i & J_t + \sum_i m z_i^2 \end{bmatrix}, \quad \mathbf{G} = \begin{bmatrix} 0 & 0 \\ 0 & J_p \end{bmatrix}, \quad \mathbf{C} = \begin{bmatrix} c_{11} & c_{12} \\ c_{12} & c_{22} \end{bmatrix}, \quad \mathbf{K} = \begin{bmatrix} k_{11} & k_{12} \\ k_{12} & k_{22} \end{bmatrix},$$

are the mass, gyroscopic, damping and stiffness matrices respectively and $\mathbf{x} = [x, \phi_y, y, -\phi_x]^T$ is the vector of the rotor degrees of freedom. We have used $-\phi_x$ instead of ϕ_x so that (9) assumes a more regular pattern. Finally the n_{ϕ_y} and $n_{-\phi_x}$ terms are given by

$$n_{\phi_y} = m \sum_{i=1}^4 \left[(\ddot{x} - 2\Omega\dot{y} - \Omega^2 x) (\phi_y \cos \alpha_i - \phi_x \sin \alpha_i) - \cos^2 \alpha_i (\ddot{\phi}_y - 2\dot{\alpha}_i \dot{\phi}_x + (\Omega^2 + 2\Omega\dot{\alpha}_i) \phi_y) \right.$$

$$\left. + \sin \alpha_i \cos \alpha_i (\ddot{\phi}_x + 2\dot{\alpha}_i \phi_y + (\Omega^2 + 2\Omega\dot{\alpha}_i) \phi_x) + \ddot{\alpha}_i \phi_x \right],$$

$$n_{-\phi_x} = m \sum_{i=1}^4 \left[(\ddot{x} - 2\Omega\dot{y} - \Omega^2 x) \phi_y \sin \alpha_i + \sin^2 \alpha_i (\ddot{\phi}_x + 2\dot{\alpha}_i \dot{\phi}_y + (\Omega^2 + 2\Omega\dot{\alpha}_i) \phi_x) \right.$$

$$\left. - (\ddot{y} + 2\Omega\dot{x} - \Omega^2 y) \phi_x \sin \alpha_i - \sin \alpha_i \cos \alpha_i (\ddot{\phi}_y - 2\dot{\alpha}_i \dot{\phi}_x + (\Omega^2 + 2\Omega\dot{\alpha}_i) \phi_y) \right].$$

Coupled with (9) are the equations of motion for the balancing balls which are

$$\begin{aligned} \ddot{\alpha}_i + c_b \dot{\alpha}_i = & \left((\ddot{x} + z_i \ddot{\phi}_y) - 2\Omega (\dot{y} - z_i \dot{\phi}_x) - \Omega^2 (x + z_i \phi_y) \right) \sin \alpha_i \\ & - \left((\ddot{y} - z_i \ddot{\phi}_x) + 2\Omega (\dot{x} + z_i \dot{\phi}_y) - \Omega^2 (y - z_i \phi_x) \right) \cos \alpha_i, \quad \text{for } i = 1, \dots, 4. \end{aligned} \quad (10)$$

We note that by taking $m = 0$ in (9), we recover the equations of motion for a four degree of freedom rotor in the rotating frame [9]. Similarly, by setting the tilt angles $\phi_x = \phi_y \equiv 0$, the system reduces to the equations of motion for the planar automatic balancer [4].

It is also worth remarking that there are certain asymmetries in the n_{ϕ_y} and $n_{-\phi_x}$ terms corresponding to the $\mathcal{O}(\delta)$ moments of the balancing balls. These arise because of the inherently asymmetrical nature of an Euler angle formulation. With reference to Fig. 2, we recall that ϕ_x is a rotation about the body ξ axis while ϕ_y is taken, not about the body η axis, but about an intermediate y' axis. With the standard rotordynamic assumptions of small tilt angles and small eccentricities these asymmetries do not survive the linearisation process. Here however, where the lever arm of the race cannot be neglected, extra terms including these asymmetries are present [11].

3 Steady state bifurcation analysis

In this section we consider the stability of the steady state solutions of the system given by equations (9-10). In order to simplify the bifurcation analysis, we shall restrict attention to a symmetric subsystem which displays all the primary features of the autobalancing process. A situation that is common in practice occurs when the rotor's centre of mass is located at the midspan and both supports are identical, so that

$$k_1 = k_2 = k, \quad c_1 = c_2 = c, \quad l_1 = l_2 = l, \quad \text{which leads to } k_{12} = c_{12} = 0.$$

With this set-up, the lateral and inclinational motions of the rotor remain coupled, but only through the motion of the balancing balls. In addition, we assume $z_{1,2} = -z_{3,4} = z$, so that the autobalancing planes are equidistant from the midspan.

The rest of this section is organised as follows: in Section 3.1 we obtain the steady state solutions, noting various conditions governing their existence, and in Section 3.2 we use the continuation package AUTO [12] to compute bifurcation diagrams showing the boundaries of stability in various parameter planes.

3.1 Steady state solutions

Steady state solutions are obtained by setting all time derivatives in the equations of motion (9-10) to zero. Moreover, if we also set the vibrational coordinates $(x, y, \phi_x, \phi_y) = \mathbf{0}$, we arrive at the following conditions for a balanced steady state

$$\begin{aligned} \cos \alpha_1 + \cos \alpha_2 + \cos \alpha_3 + \cos \alpha_4 &= s_x, \\ \sin \alpha_1 + \sin \alpha_2 + \sin \alpha_3 + \sin \alpha_4 &= s_y, \\ \cos \alpha_1 + \cos \alpha_2 - \cos \alpha_3 - \cos \alpha_4 &= c_x, \\ \sin \alpha_1 + \sin \alpha_2 - \sin \alpha_3 - \sin \alpha_4 &= c_y, \end{aligned} \quad (11)$$

where

$$s_x = \frac{-\epsilon \cos \beta}{m}, \quad s_y = \frac{-\epsilon \sin \beta}{m}, \quad c_x = \frac{-\chi (J_t - J_p)}{mz}, \quad c_y = 0.$$

These are precisely the conditions for equilibrium between the centrifugal forces and moments acting on the rotor due to the imbalance and balancing balls [8]. By rewriting the above equation with respect to

the average and differential angular displacements within each race, we find that

$$\begin{aligned}\cos \hat{\alpha}_{12} \cos \bar{\alpha}_{12} &= \frac{s_x + c_x}{4}, \\ \cos \hat{\alpha}_{12} \sin \bar{\alpha}_{12} &= \frac{s_y + c_y}{4}, \\ \cos \hat{\alpha}_{34} \cos \bar{\alpha}_{34} &= \frac{s_x - c_x}{4}, \\ \cos \hat{\alpha}_{34} \sin \bar{\alpha}_{34} &= \frac{s_y - c_y}{4},\end{aligned}\tag{12}$$

where

$$\bar{\alpha}_{12} = \frac{\alpha_1 + \alpha_2}{2}, \quad \hat{\alpha}_{12} = \frac{\alpha_1 - \alpha_2}{2}, \quad \bar{\alpha}_{34} = \frac{\alpha_3 + \alpha_4}{2}, \quad \hat{\alpha}_{34} = \frac{\alpha_3 - \alpha_4}{2}.$$

Because the balls are assumed to be identical, we may without loss of generality take $0 \leq \hat{\alpha}_{12}, \hat{\alpha}_{34} \leq \frac{\pi}{2}$ and equation (12) can now be solved to give the following physically unique balanced state

$$\begin{aligned}\bar{\alpha}_{12} &= \arctan\left(\frac{s_y + c_y}{s_x + c_x}\right) + \begin{cases} 0 & \text{if } s_x + c_x \geq 0, \\ \pi & \text{if } s_x + c_x < 0. \end{cases}, \\ \hat{\alpha}_{12} &= \arccos\left(\frac{1}{4}\sqrt{(s_x + c_x)^2 + (s_y + c_y)^2}\right), \\ \bar{\alpha}_{34} &= \arctan\left(\frac{s_y - c_y}{s_x - c_x}\right) + \begin{cases} 0 & \text{if } s_x - c_x \geq 0, \\ \pi & \text{if } s_x - c_x < 0. \end{cases}, \\ \hat{\alpha}_{34} &= \arccos\left(\frac{1}{4}\sqrt{(s_x - c_x)^2 + (s_y - c_y)^2}\right).\end{aligned}\tag{13}$$

This solution exists provided that the arguments for both the arccoses have modulus less than one, which ensures that the balls have enough mass to counteract the imbalance of the system. In what follows we refer to (13) as the balanced state **B**.

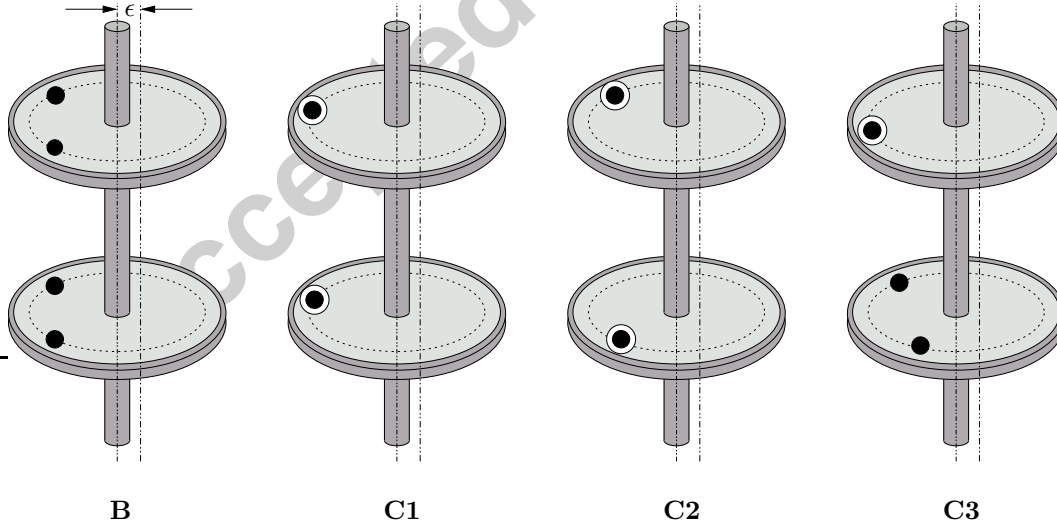


Fig. 4: Schematic diagram of the steady states for the case of a static imbalance. White surrounds denote that both balls in the race are coincident.

The steady state configurations for the special case of a rotor with a static imbalance are illustrated in Fig. 4. The balanced state **B** is shown on the left, but there are also various other steady state solutions for which the rotor remains out of balance. In these cases we consider the equation for the balls (10), which yields

$$(x + z_i \phi_y) \sin \alpha_i = (y - z_i \phi_x) \cos \alpha_i, \quad i = 1 \dots 4,\tag{14}$$

where $x + z_i\phi_y$ and $y - z_i\phi_x$, are recognised as the x and y deflections of the race centres. If for both of the races $(x + z_i\phi_y, y - z_i\phi_x) \neq \mathbf{0}$, then we may rewrite (14) as

$$\tan \alpha_i = \left(\frac{y - z_i\phi_x}{x + z_i\phi_y} \right), \quad i = 1 \dots 4,$$

with solutions

$$\alpha_1 = \alpha_2 + p\pi, \quad \alpha_3 = \alpha_4 + q\pi, \quad p, q \in \mathbb{Z}.$$

Therefore the balls in each race are either *coincident*, or *in-line* with the race centre and opposite each other. For example, in state **C1** all the balls have the same angle and this configuration results in the excitation of a cylindrical whirl. For state **C2**, the balls in each race are again coincident but there are now two distinct angular displacements. This arrangement generates a couple imbalance and leads to a conical type whirl. The inline states will not be discussed further because they are found to be always unstable and are never involved in bifurcations with the balanced state.

Next we consider the state **C3**, in which $(x + z_i\phi_y, y - z_i\phi_x) = \mathbf{0}$ is satisfied by one of the two races, so that its centre stays fixed at the undeflected position. The balls within this fixed race are now not constrained by equation (14), although the balls in the opposing race are again either coincident or inline. As an example, the arrangement for **C3** depicted in Fig. 4 shows coincident balls in the top race while the bottom race balls are split. The corresponding state, where the roles of the races are swapped, is physically equivalent, because the symmetry between the two races is preserved by a static imbalance. However, this will not be the case for a general imbalance, as we shall discuss in section 3.2.2. Finally, we note that if $(x + z_i\phi_y, y - z_i\phi_x) = \mathbf{0}$, for both of the races, then we are again led to the balanced state **B**, which has been covered previously.

3.2 Numerical continuation

For the remainder of this study we shall consider a rotor with the following inertial and stiffness parameters

$$\begin{aligned} J_t &= 3.25, & J_p &= 0.5, & l &= 3, \\ k_{11} &\equiv 1, & k_{12} &= 0, & k_{22} &= 9. \end{aligned} \tag{15}$$

These values are based on a solid cylindrically shaped rotor with a height of six times its radius. A rotating machine on compliant bearings with this geometry would typically undergo a two-plane balancing procedure before going into service. The approximate natural frequencies for the cylindrical and conical modes occur respectively at

$$\Omega_1 = \sqrt{\frac{k_{11}}{M}} \equiv 1, \quad \text{and} \quad \Omega_2 = \sqrt{\frac{k_{22}}{J_t - J_p}} \simeq 1.81, \tag{16}$$

and we shall now investigate the results for both the static and dynamic imbalance cases.

3.2.1 Static Imbalance

As mentioned above, a static imbalance occurs when the principal axis is displaced, but parallel to, the rotation axis so that there is a shaft eccentricity $\epsilon \neq 0$, but no shaft misalignment $\chi = 0$. For this special case, we are able to recover all the bifurcations and steady state solutions that have been found previously in the studies of a planar automatic balancer [3, 4]. However, because our model includes the extra inclinational degrees of freedom, the rotor is now able to destabilise via out of plane motions, and so, the steady states will necessarily have smaller regions of stability.

In Fig. 5 we present results for the following parameters

$$\begin{aligned} \epsilon &= 0.01, & \chi &= 0, & (\beta &= 0), \\ z &= 2, & c_b &= 0.01, & \text{and} & c = 0.01, \\ \text{so that} & & & & & \\ c_{11} &= 0.02, & c_{12} &= 0, & c_{22} &= 0.18. \end{aligned} \tag{17}$$

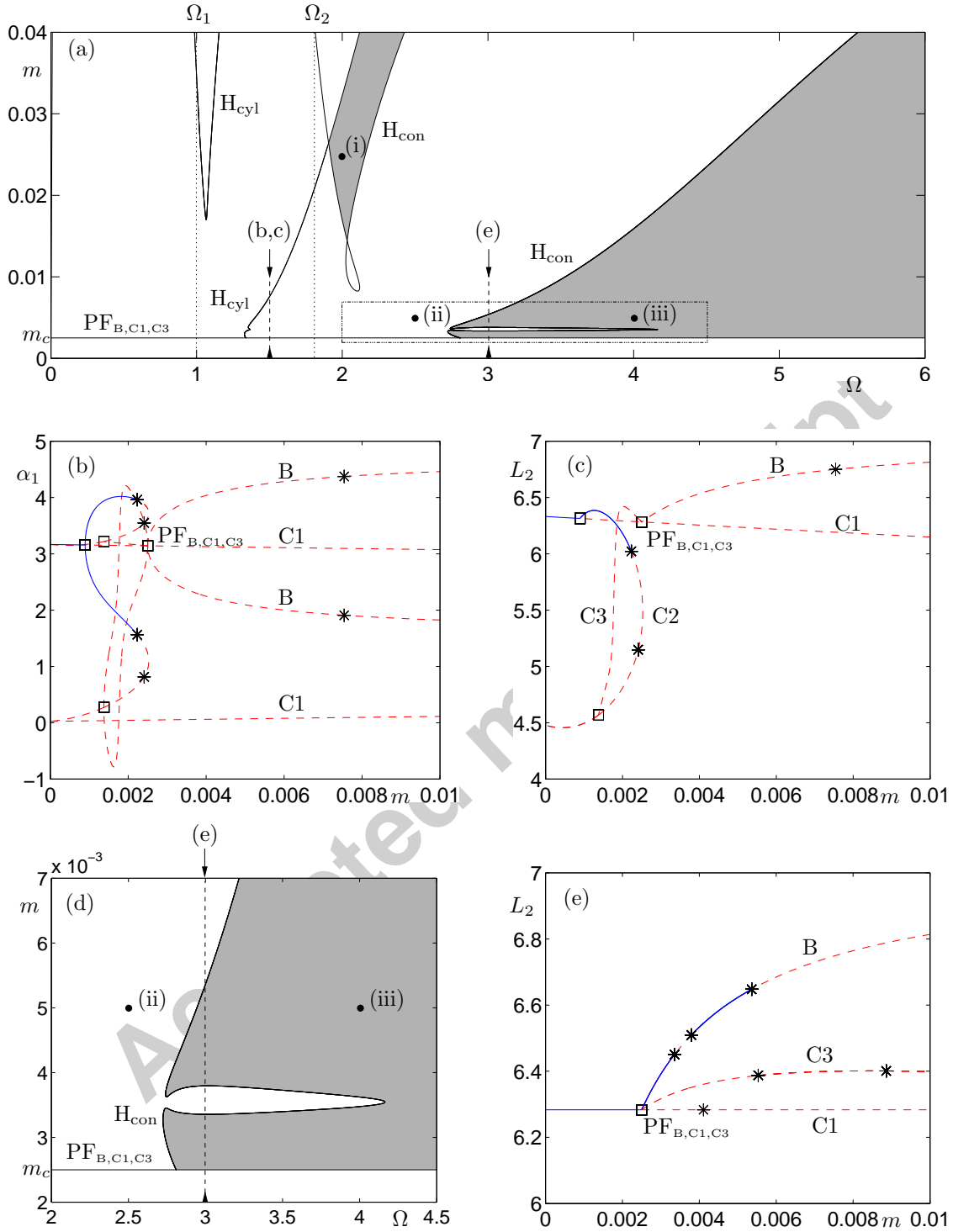


Fig. 5: Bifurcation diagrams in the (Ω, m) -plane showing curves of the (degenerate) pitchfork PF and Hopf bifurcations H which involve the balanced state **B**, (a) and (d). We take $\epsilon = c = c_b = 0.01$, with the other parameters given by (15-17). The shaded regions correspond to a stable balanced state, and the subscripts for the Hopf bifurcations denote which mode is involved. Numerical simulations at the points indicated by a \bullet are presented in Fig. 11. One-parameter diagrams in m for $\Omega = 1.5$ are shown in (b) and (c), with norms given by α_1 and L_2 respectively, and labels for the steady states described as in Fig. 4. Panel (e) shows the one-parameter bifurcation diagram for $\Omega = 3$.

For this value of the eccentricity, the balanced state \mathbf{B} exists provided that

$$m \geq m_c := \frac{\epsilon}{4} = 0.0025, \quad (18)$$

where m_c is the critical value of the ball mass. We also note that the balancing planes are appropriately spaced, and that the race and supports have low damping values, which match those in [3, 4]. Figure 5(a) shows the results of a two-parameter bifurcation analysis upon variation of the dimensionless parameters Ω and m , whilst we keep the other parameters fixed. The shaded regions correspond to the existence of a stable balanced state \mathbf{B} , although as we shall discuss in section 4, other less desirable stable states may coexist in these regions. For masses of the balls which satisfy $m \geq m_c$ the balanced state \mathbf{B} always exists, but it is not necessarily stable. The curves marked H_{cy1} and H_{con} are Hopf bifurcations of \mathbf{B} , at which oscillations are induced by the cylindrical and conical modes respectively. In a planar analysis only the H_{cy1} curves are present, and as such, they are always accompanied by a change in stability. Here with the inclusion of the inclinational degrees of freedom, the stability of \mathbf{B} is predominately determined by the H_{con} curves, at which the conical type oscillations, are either created or destroyed.

For large values of Ω , the balanced state \mathbf{B} stabilises in a Hopf bifurcation H_{con} and there is also a secondary region of stability, for sufficiently large values of m , at rotation speeds just above the natural frequency Ω_2 . We also draw attention to the similarities between the shape of the two Hopf curves H_{cy1} and H_{con} , suggesting that there is in some sense, a duality between the lateral and inclinational dynamics of the automatic balancer.

The one-parameter bifurcation diagrams of Figs. 5(b) and (c) show the result of increasing m through m_c for $\Omega = 1.5$, which is a value of the rotation speed that lies in between the natural frequencies of the rotor. The angular displacement α_1 is used as the solution measure in Fig. 5(b), and we see that an unstable balanced state \mathbf{B} is born at $m = m_c$ in a pitchfork bifurcation involving the unstable coincident state $\mathbf{C1}$. Note that the two copies of the balanced state \mathbf{B} come from interchanging the ball positions, for example $\alpha_1 \leftrightarrow \alpha_2$. In Fig. 5(c) we plot the same bifurcation diagram as shown in panel (b) but instead we use the Euclidean norm L_2 . Here only one copy of each physically unique state is generated, and we can see that the balanced state \mathbf{B} is in fact produced at a degenerate pitchfork bifurcation involving the states $\mathbf{C1}$ and $\mathbf{C3}$.

Next we consider the situation for the supercritical regime where $\Omega > \Omega_2$. Figure 5(d) is an enlargement of our region of interest and panel (e) shows a one parameter scan as we increase m through m_c , for a fixed rotation speed of $\Omega = 3$. Again we find that the balanced state \mathbf{B} is born at a degenerate pitchfork bifurcation involving states $\mathbf{C1}$ and $\mathbf{C3}$, but in contrast with the situation for subcritical rotation speeds, the coincident state $\mathbf{C1}$ and the bifurcating balanced state \mathbf{B} are now both stable. Note also, that the balanced state changes stability through a series of three further Hopf bifurcations, which is in agreement with the vertical slice taken through panel (d) at $\Omega = 3$.

Now let us consider some stability diagrams similar to Fig. 5(a), in which we vary other dimensionless parameters. We take $m = 0.025$ so that condition (18) needed for balance is satisfied, and the values for the other parameters when fixed, are again given by (15) and (17).

In Fig. 6 we display some two-parameter stability charts upon variation of the eccentricity ϵ , the support damping c , and the race damping c_b , as the rotation speed Ω is increased. Here, we are again able to recover the H_{cy1} curves which are present in the planar analyses, but as before the H_{con} bifurcations have more influence on the stability of the balanced state. We also highlight some of the same features which were present in Fig. 5, namely: the stabilisation of the balanced state through a H_{con} Hopf bifurcation for high enough rotation speeds, the smaller secondary stable region at rotation speeds just above Ω_2 , and most notably in panel (c) the similarity between the shapes of the H_{cy1} and H_{con} curves.

Figure 7 shows the eccentricity ϵ , plotted against Ω , whilst we also vary the ball mass so that $m = 4m_c = \epsilon$. Thus, for any given value of the eccentricity, the balls have a mass which is four times the minimum amount that is required to balance the system. A logarithmic scale is used for the vertical axis so that a wide range of eccentricities can be considered. Here, the main area of interest occurs for small eccentricities and supercritical rotation speeds where there is a large connected stable region. We also note that the H_{con} curve, which bounds this region, asymptotes towards $\Omega = \Omega_2$ as $\epsilon \rightarrow 0$ so that there is no stable region in the subcritical regime.

Finally, before moving on to a general dynamic imbalance, we shall briefly discuss the case of a couple imbalance, for which there is a shaft misalignment $\chi \neq 0$ but no shaft eccentricity $\epsilon = 0$. The steady states for this case are illustrated schematically in Fig. 8. The only difference between the static imbalance

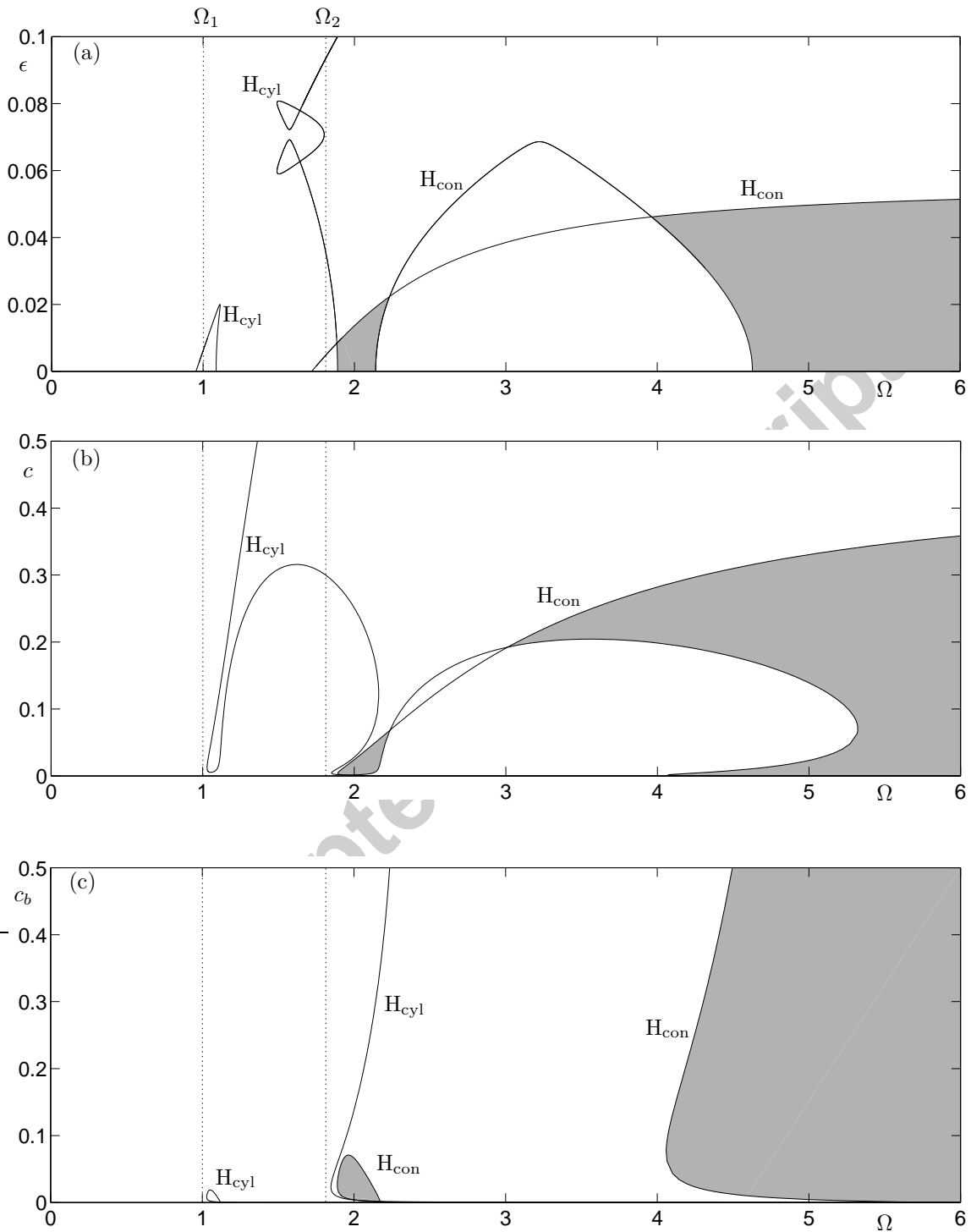


Fig. 6: Two-parameter bifurcation diagrams, upon variation of the parameters: ϵ against Ω (a), c against Ω (b), and c_b against Ω (c). The shaded regions correspond to a stable balanced state \mathbf{B} , and Hopf bifurcations H are shown with subscripts indicating the mode of oscillation. Parameters when fixed are $m = 0.025$, $\epsilon = c = c_b = 0.01$, with the other values specified in the text.

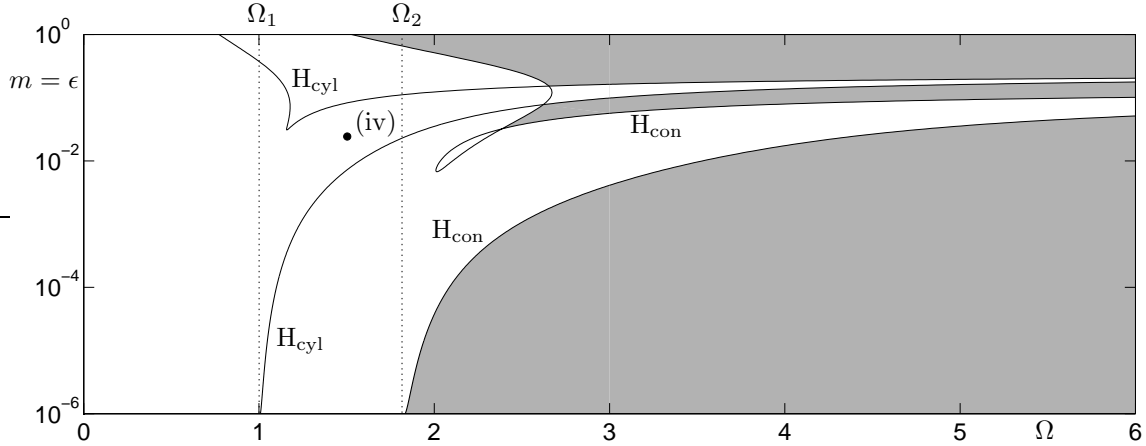


Fig. 7: Diagram showing stable regions of the balanced state **B** upon variation of the parameters ϵ against Ω , whilst m is also varied so that $m = \epsilon$. The vertical scale is logarithmic and $c = c_b = 0.01$.

steady states of Fig. 4 is that here the bottom race has been rotated through an angle of π radians. Again, the symmetry between the two races is preserved by this type of imbalance, and the balanced state **B** is always born in a degenerate pitchfork bifurcation involving the coincident states **C1** and **C3**. Moreover if the misalignment parameter χ , is appropriately chosen so that we again have $m_c = 0.0025$, the results shown in Fig. 5(a) for a static imbalance can be recovered. Thus, there is an equivalence between the properties of the automatic balancer for a pure eccentricity and for a pure misalignment, and we shall not provide any explicit bifurcation diagrams for the couple imbalance case.

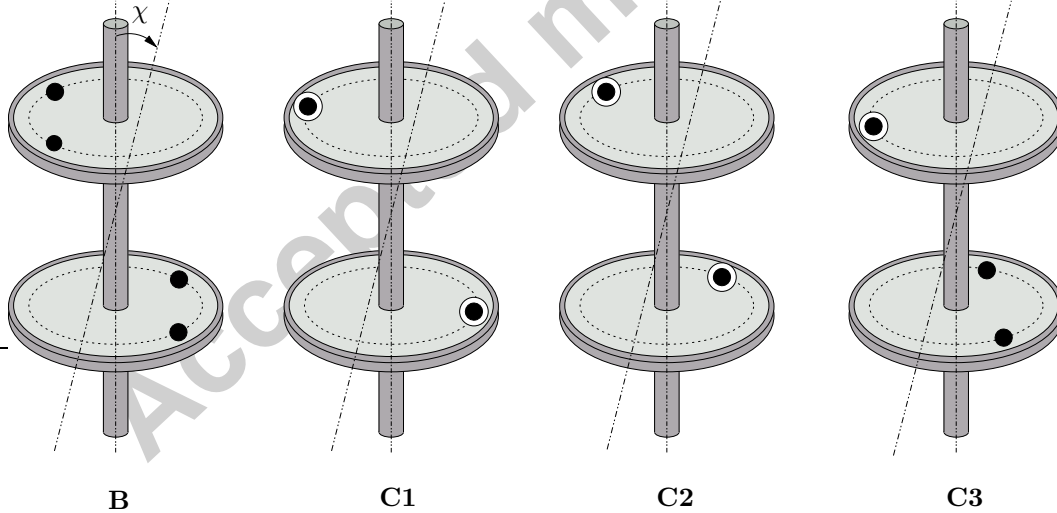


Fig. 8: Schematic diagram of the steady states for the case of a couple imbalance. White surrounds again indicate that both balls in the race are coincident.

3.2.2 Dynamic Imbalance

A dynamic imbalance arises when there is both a shaft eccentricity $\epsilon \neq 0$, and a shaft misalignment $\chi \neq 0$. A phase angle β must also be included to describe the difference between the directions of the two imbalances.

The parameter set which was given in (15) and (17) is used again, except that we change the imbalance

characteristics to

$$\epsilon = 0.005, \quad \chi = 0.005, \quad \beta = 1.$$

The critical mass for the balls m_c , is now given by

$$m_c := \max \left\{ \frac{1}{4} \sqrt{\left(\epsilon \cos \beta \pm \frac{\chi (J_t - J_p)}{z} \right)^2 + (\epsilon \sin \beta)^2} \right\} \simeq 0.00261, \quad (19)$$

which is a similar value to that in the static imbalance case of the previous section.

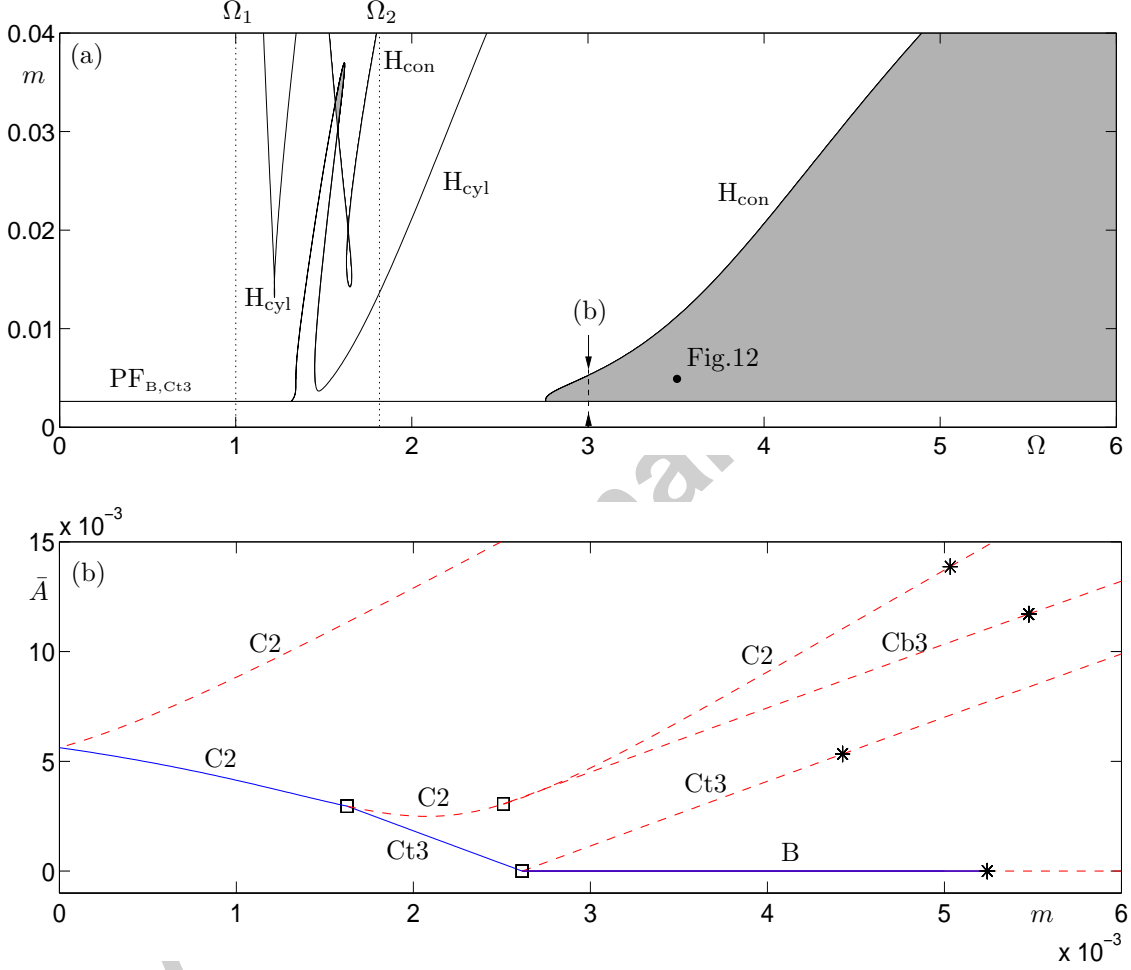


Fig. 9: Panel (a) is a bifurcation diagram in the (Ω, m) -plane showing curves of the pitchfork PF and Hopf bifurcations H which involve the balanced state \mathbf{B} . Parameters when fixed are, $\epsilon = \chi = 0.005$, $\beta = 1$, and $c = c_b = 0.01$ with the other values specified in the text. The shaded region corresponds to a stable balanced state, and the subscripts for the Hopf bifurcations denote which mode is involved. Numerical simulations at the point highlighted by a \bullet are presented in Fig. 12. A one-parameter diagram in m for $\Omega = 3$ is shown in (b), with norm given by \bar{A} .

In Fig. 9(a) we provide a two-parameter bifurcation diagram upon the variation of the ball mass m and the rotation speed Ω . Qualitatively the graph is similar to the static case of Fig. 5(a), in that the balanced state also stabilises in a Hopf bifurcation H_{con} , for high enough rotation speeds in the supercritical regime. However the secondary stable region has now almost disappeared, and we see a sharp upward spike in the lower H_{cyl} curve which is indicative of mixing between the cylindrical and conical modes. In panel (b) we scan vertically through Fig. 9(a) holding the rotation speed fixed at

$\Omega = 3$, while increasing the ball mass m through m_c . In this diagram we use the norm \bar{A} defined by

$$\bar{A} = \frac{1}{2} \left(\sqrt{(x + \phi_y)^2 + (y - \phi_x)^2} + \sqrt{(x - \phi_y)^2 + (y + \phi_x)^2} \right). \quad (20)$$

Physically this measure corresponds to the average vibration level at the points on the shaft that are a unit length from the rotor centre. We see that the degenerate pitchfork bifurcation which was present for the static imbalance case has been split into three separate non-degenerate pitchforks. For a generic dynamic imbalance this unfolding occurs because the symmetry between the two races has been broken. As a consequence, the unbalanced steady state **C3** separates into two physically different cases. The configuration with coincident balls in to top race is called **Ct3**, whereas the corresponding state with the bottom race balls coincident is **Cb3**. We find that the symmetry and resulting degenerate bifurcation is only preserved when there is a pure static or couple imbalance or if the phase is such that $\cos \beta = 0$. In all these cases there is no component of the shaft eccentricity which lies in the direction of the misalignment. Thus from (13) we can see that $\hat{\alpha}_{12} \equiv \hat{\alpha}_{34}$ and so the balanced state **B** is born from a state where the balls in both races are coincident.

Finally in Fig. 10 we provide a two-parameter bifurcation analysis as we vary the support damping c versus Ω (a), and the race damping c_b versus Ω (b). Again we choose $m = 0.025$ so that condition (19) for the existence of the balanced state is satisfied. By comparison with Fig. 6 we note that in both cases the secondary stable regions have been lost. Also the stable region for high rotation speeds and high support damping c is dramatically reduced.

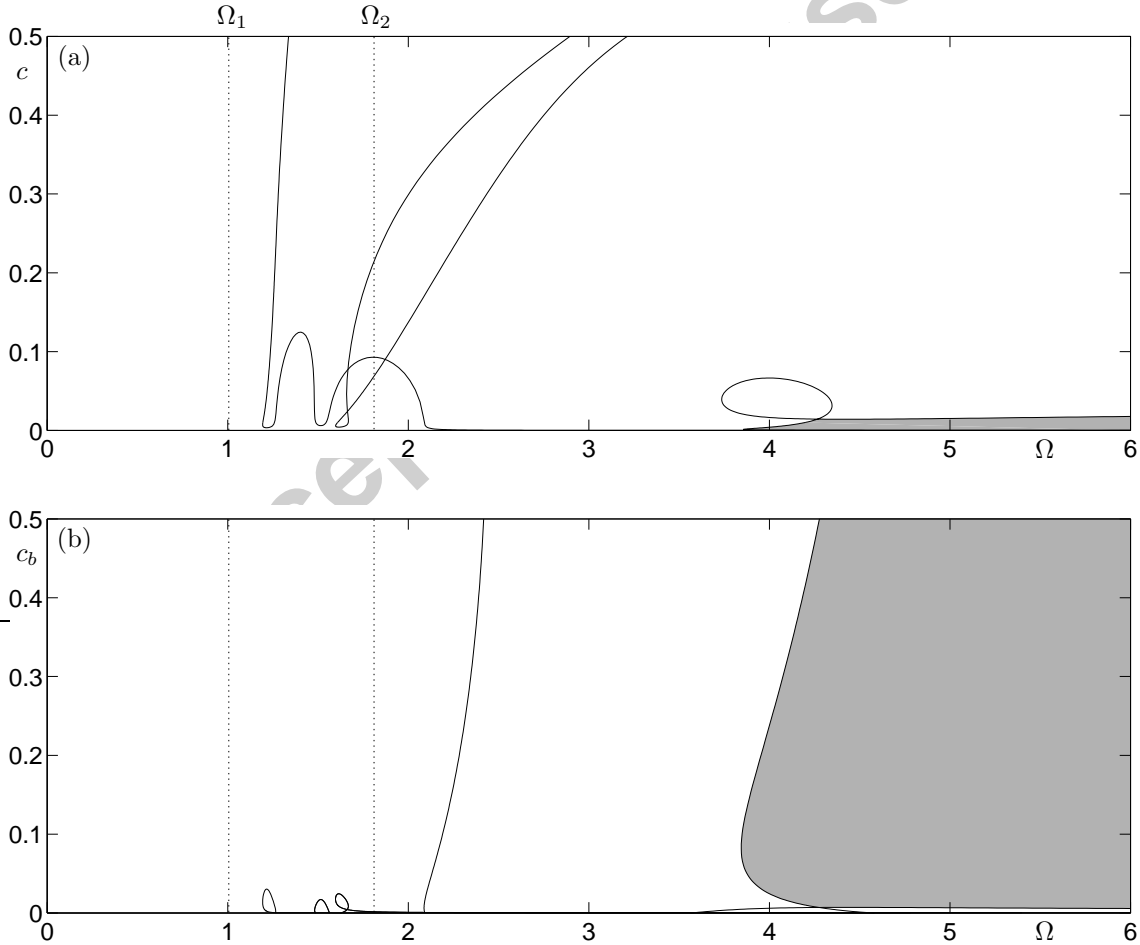


Fig. 10: Two-parameter bifurcation diagrams, upon variation of the parameters, c versus Ω (a), and c_b versus Ω (b). The shaded regions correspond to a stable balanced state **B**. Parameters when fixed are $m = 0.025$, $\epsilon = \chi = 0.005$, $\beta = 1$, and $c = c_b = 0.01$ with the other values specified in the text.

4 Numerical Simulation

We build on the bifurcation analysis of the previous section by presenting some results which illustrate the important dynamics of the automatic ball balancer (ABB). Here we use the `Matlab` routine `ode45` to perform a direct numerical integration of the equations of motion (9-10), which were derived in section 2. As a check, we note that our simulations agree with those of [3, 4] for appropriate choices of the parameters and initial conditions.

Figure 11 shows the effect of varying the system parameters for the static imbalance case that was discussed in section 3.2.1. The positions in parameter space of these runs are highlighted in Figs. 5 and 7. We plot the vibration measure \bar{A} against the dimensionless time t , here the black curve represents the motion of the rotor with the ABB and the grey curve the motion of the rotor without the ABB. The initial conditions for all four plots are the same and are given by

$$\begin{aligned} \alpha_1 = -\alpha_2 = \alpha_3 = -\alpha_4 = \pi/2, \text{ and} \\ (x, y, \phi_x, \phi_y) = (\dot{x}, \dot{y}, \dot{\phi}_x, \dot{\phi}_y) = (\dot{\alpha}_1, \dot{\alpha}_2, \dot{\alpha}_3, \dot{\alpha}_4) = \mathbf{0}. \end{aligned} \quad (21)$$

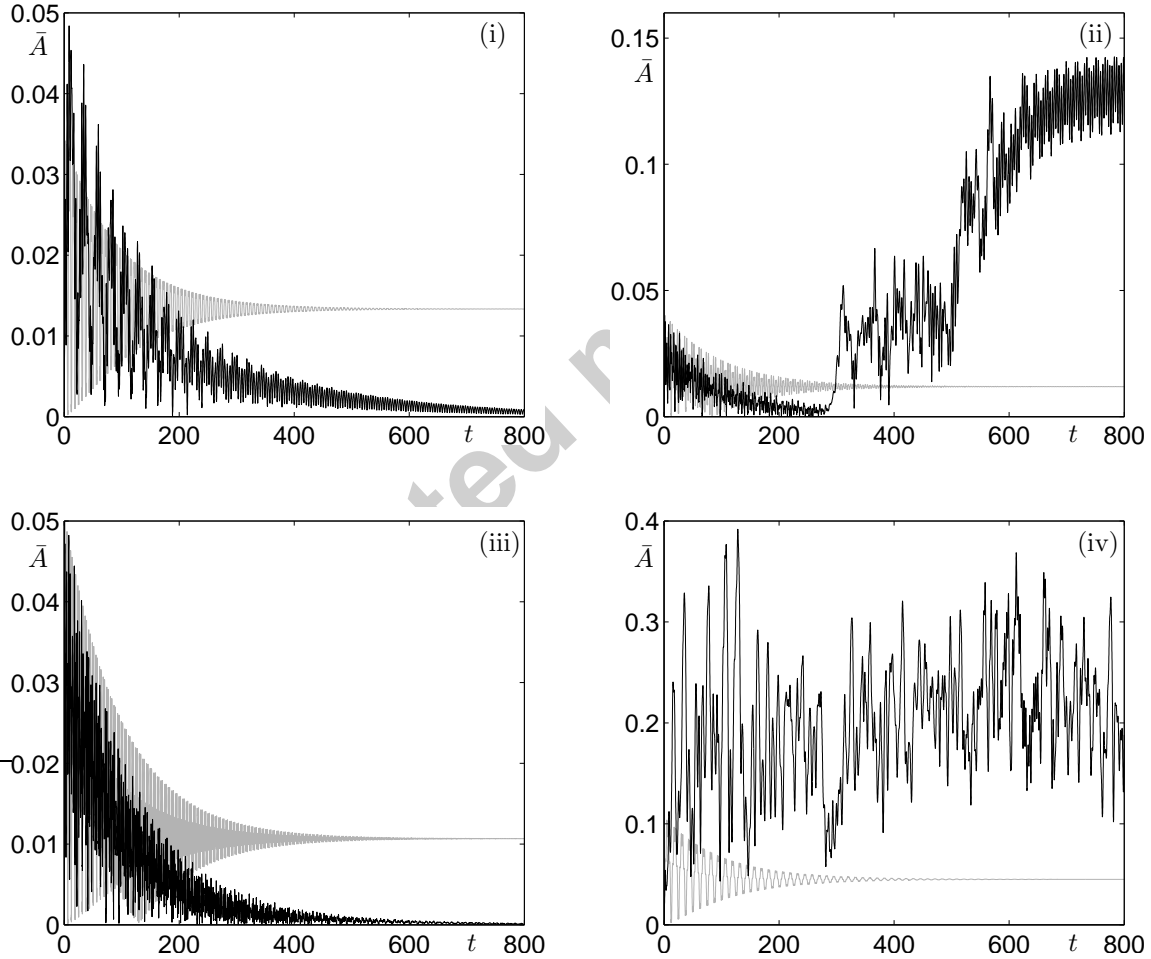


Fig. 11: Numerical simulations showing vibration levels for the static imbalance case with low damping $c = c_b = 0.01$. Initial conditions are fixed so that the rotor begins at rest and the balls in each race are on opposite sides with $(\alpha_1, -\alpha_2) = (\alpha_3, -\alpha_4) = \pi/2$. Values of Ω , ϵ and m are fixed at $(\Omega, \epsilon, m) = (2.0, 0.01, 0.025)$ (a), $(2.5, 0.01, 0.005)$ (b), $(4.0, 0.01, 0.005)$ (c), and $(1.5, 0.025, 0.025)$ (d). These points are specified in parameter space by a \bullet in Figs. 5 and 7.

Therefore the rotor starts at rest in the undeflected position and the balls are initially stationary (with respect to the rotating frame) and are placed on opposite sides to each other so that they do not add

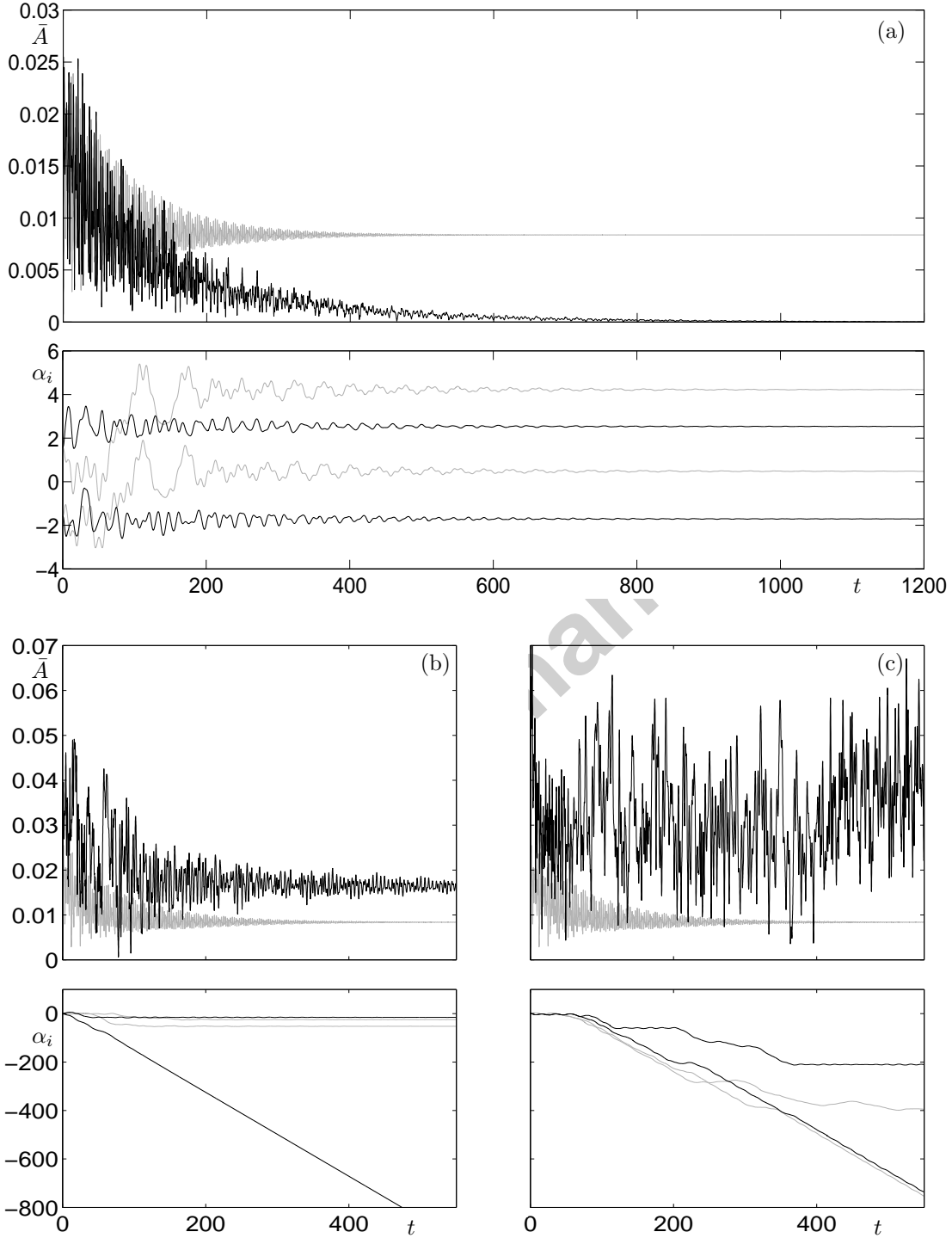


Fig. 12: Numerical simulations for the dynamic imbalance $(\epsilon, \chi, \beta) = (0.005, 0.005, 1.0)$ showing vibration levels \bar{A} above the ball positions α_i . The parameter set used is the same as that in section 3.2.2 with Ω and m fixed at $(\Omega, m) = (3.5, 0.005)$. This position is also highlighted by a \bullet in Fig. 9. Initial conditions are $(\alpha_1, -\alpha_2) = (\alpha_3, -\alpha_4) = \pi/2$ (a), $(\alpha_1, -\alpha_2) = \pi/3$, $(\alpha_3, -\alpha_4) = 2\pi/3$ (b) and $(\alpha_1, \alpha_2) = 0$, $(\alpha_3, \alpha_4) = \pi$ (c).

to the imbalance of the rotor. Panel (i) shows the simulation for $(\Omega, \epsilon, m) = (2, 0.01, 0.025)$ which, with reference to Fig. 5, lies in the secondary region of stable balanced operation, at a rotation speed just above the natural frequency Ω_2 . We note that although the autobalancing state is eventually achieved, the transients produce slightly higher levels of initial vibrations. Also, if we perturb the initial conditions so that the shaft is slightly tilted, we find that the rotor can easily destabilise into a periodic type motion with significantly worse levels of vibration (not shown but qualitatively similar to that of (ii)). This effect may be understood by considering the results of Fig. 9, where we commented on the disappearance of the secondary stable region upon the introduction of a shaft misalignment. The initial tilt of the rotor leads to a motion of the balls that produces a small couple imbalance, which in turn destabilises the operation of the ABB.

Figure 11 (ii) shows the time profile for $(\Omega, \epsilon, m) = (2.5, 0.01, 0.005)$. This point lies outside the region of stability for the balanced state **B**, however the transient response dies down to a very low vibration level before eventually destabilising into periodic motion. This type of behaviour is typical of the dynamics near a saddle type fixed point when there are symmetrical initial conditions. In panel (iii) our parameters are $(\Omega, \epsilon, m) = (4, 0.01, 0.005)$, which lies in the larger primary region of stable balanced operation. For this case, balance is achieved after $t \approx 400$ and the transient period for both curves are approximately the same. Moreover the dynamics here are more robust than in (i) to perturbations in the initial tilt of the rotor. Again, with particular reference to Figs. 5 (a) and 9 (a), we observe that the primary region of stability is not greatly influenced by the inclusion of a couple imbalance. Thus initial motions of the balls, which cause small inclinational motions, tend not to destabilise the device. Finally, in panel (iv) we illustrate the behaviour for $(\Omega, \epsilon, m) = (1.5, 0.025, 0.025)$ which, as shown in Fig. 7, lies well outside any region of balanced operation. This is a very undesirable state as the rotor now appears to undergo chaotic motion and reaches levels of vibration which are far higher than that for the rotor without an ABB mechanism.

Now we turn to the effect that the initial conditions have on the operation of the ABB. It was found that there was little sensitivity to typical variations in the initial values of the vibrational coordinates (x, y, ϕ_x, ϕ_y) or their velocities $(\dot{x}, \dot{y}, \dot{\phi}_x, \dot{\phi}_y)$, however the initial value of the ball positions α_i can have a dramatic impact on the outcome of the system. We consider the dynamic imbalance case of section 3.2.2 where $(\epsilon, \chi, \beta) = (0.005, 0.005, 1.0)$. In particular we take $(\Omega, m) = (3.5, 0.005)$, which is indicated in Fig. 9 and lies in the stable balanced region. We display in Fig. 12 the vibration level \bar{A} for the rotor with and without the ABB mechanism and the angular displacement of the balancing balls α_1, α_2 (black curves) and α_3, α_4 (grey curves) are shown underneath. Panel (a) illustrates the results for the same initial conditions that were used for Fig. 11; namely those given by (21). Here the balls get attracted to the balanced state **B** with angular positions α_i given by (13).

In panel (b) we take the initial conditions $\alpha_1 = -\alpha_2 = \pi/3$, $\alpha_3 = -\alpha_4 = 2\pi/3$, this has the effect of increasing the initial couple imbalance of the rotor. Here the device settles down to a periodic motion where the vibration level is about twice that of the rotor without the ABB. We find that one of the balls in the top race lags behind the rotor with $\dot{\alpha} = -\Omega$. Thus this ball only performs one revolution for every two of the rotor. Note that a model which included partitions of the race [13] or allowed for collisions between balls would prevent such dynamics. Finally in Fig. 12 (c) we consider starting conditions where the initial couple balance is maximised so that $\alpha_1 = \alpha_2 = 0$, and $\alpha_3 = \alpha_4 = \pi$. In this case the rotor appears to undergo a chaotic motion and the vibration level of the rotor is an order of magnitude worse.

5 Conclusion

We have provided the first nonlinear bifurcation analysis of a two-plane automatic balancer for rigid rotors. It has been demonstrated that the use of rotating coordinates enables an autonomous formulation for the equations of motion. Two-parameter stability charts obtained by numerical continuation show that the considered device can effectively eliminate imbalances arising from both shaft eccentricity and shaft misalignment. However, the balancing process only works for sufficiently high rotation speeds above the second critical frequency [8].

In our investigations, we have found all the bifurcations which appear in the planar analysis of the ABB [3, 4], together with additional bifurcations that occur as a result of the out-of-plane motions. Furthermore, we have highlighted how the symmetry properties of the imbalance affects the degeneracy of the bifurcation at which the balanced state is born.

In addition, we have presented numerical simulations which show the coexistence of the balanced state with other less desirable dynamics. Here as expected, the probability of successful operation is maximised by releasing the balls from directly opposite points on the race so that the initial imbalance is not increased.

The model introduced in this paper has a number of assumptions that may not be valid for an autobalancer operating on a real machine. We plan to continue the present work by investigating the performance of the automatic balancer on rotors which have asymmetric support characteristics or where the balancing planes are not equidistant from the midspan. Also more research needs to be carried out in order to determine the influence of ball-race interactions and rotor flexibility on the autobalancing process.

However it is clear that the ABB is a highly nonlinear device, and so the regions of its stability depend in a non trivial way on the parameters of the system. As a result, we expect that the methods provided here will influence the design requirements for the ABB, in order that it may successfully emulate the two-plane balancing procedure.

6 Acknowledgements

DJR gratefully acknowledges the support from a CASE award provided by the EPSRC and Rolls-Royce plc.

References

- [1] E. Thearle, A new type of dynamic-balancing machine, *Transactions of the ASME* **54**(APM-54-12) (1932) 131-141.
- [2] J. Lee and W. K. Van Moorhem, Analytical and experimental analysis of a self compensating dynamic balancer in a rotating mechanism, *ASME Journal of Dynamic Systems, Measurement and Control* **118** (1996) 468-475.
- [3] J. Chung and D. S. Ro, Dynamic analysis of an automatic dynamic balancer for rotating mechanisms. *Journal of Sound and Vibration* **228**(5) (1999) 1035-1056.
- [4] K. Green, A. R. Champneys, and N. J. Lieven, Bifurcation analysis of an automatic dynamic balancer for eccentric rotors. *Journal of Sound and Vibration* **291** (2006) 861-881.
- [5] M. Hedaya and R. Sharp, An analysis of a new type of automatic balancer, *Journal of Mechanical Engineering Science* **19**(5) (1977) 221-226.
- [6] J. Chung and I. Jang, Dynamic response and stability analysis of an automatic ball balancer for a flexible rotor. *Journal of Sound and Vibration* **259**(1) (2003) 31-43.
- [7] C.-P. Chao, Y.-D. Huang, and C.-K. Sung, Non-planar dynamic modeling for the optical disk drive spindles equipped with an automatic balancer. *Mechanism and Machine Theory* **38** (2003) 1289-1305.
- [8] L. Sperling, B. Ryzhik, Ch. Linz and H. Duckstein, Simulation of two-plane automatic balancing of a rigid rotor, *Mathematics and Computers in Simulation* **58** (2002) 351-365.
- [9] G. Genta, *Dynamics of Rotating Systems*. Springer, New York (2005).
- [10] D. J. Rodrigues, A. R. Champneys, M. I. Friswell and R. E. Wilson, Automatic balancing of a rigid rotor with misaligned shaft, *Journal of Applied Mechanics and Materials* **5-6** (2006) 231-236.
- [11] G. Genta, C. Delprete and E. Busa, Some considerations on the basic assumptions in rotordynamics, *Journal of Sound and Vibration* **227**(3) (1999) 611-645.
- [12] E. Doedel, A. Champneys, T. Fairgrieve, Y. Kusnetsov, B. Sanstede, and X. Wang, AUTO97: Continuation and bifurcation software for ordinary differential equations, <http://indy.cs.concordia.ca/auto/main.html>, 1997.

- [13] K. Green, A. R. Champneys, M. I. Friswell, and A. M. Muñoz, Investigation of a multi-ball automatic dynamic balancing mechanism for eccentric rotors, *Philosophical Transactions of the Royal Society A*, Theme Issue 'Experimental nonlinear dynamics I. Solids' (2007).

Accepted manuscript